# Silicone-Rubber-Based Tactile Sensors for the Measurement of Normal and Tangential Components of the Contact Force

**Alberto D'Amore,[1] Giuseppe De Maria,[2] Luigi Grassia,[1] Ciro Natale,[2] Salvatore Pirozzi[2]**

[1]*Department of Aerospace and Mechanical Engineering, The Second University of Naples, Aversa (Caserta) 81031, Italy*
[2]*Department of Information Engineering, The Second University of Naples, Aversa (Caserta) 81031, Italy*

Received 28 April 2011; accepted 28 April 2011
DOI 10.1002/app.34790
Published online 11 August 2011 in Wiley Online Library (wileyonlinelibrary.com).

**ABSTRACT:** This article presents the developmental process of a new tactile sensor. The sensor was based on the use of light-emitting diode (LED) phototransistor couples and a silicone rubber layer positioned above the optoelectronics devices. The optoelectronic components were organized in a matrix structure. For each couple, the LED illuminated the reflective surface, which coincided with the bottom facet of the deformable layer. Practically, the deformable layer transduced an external force into a displacement variation of its bottom facet through its stiffness. An external force applied to the deformable layer produced local variations of the bottom surface of the elastic material, and the couples of optical devices measured the vertical deformations in a discrete number of points. In particular, these vertical displacements produced a variation of the reflected light intensity and, accordingly, of the photocurrent measured by the photodetector. The realized prototype was designed and optimized through finite element analysis. A calibration procedure is also presented, whose results demonstrate the ability of the sensor to reconstruct the contact point and also the normal and tangential components of the contact force. © 2011 Wiley Periodicals, Inc. J Appl Polym Sci 122: 3758–3770, 2011

**Key words:** rubber; sensors; silicones

## INTRODUCTION

Researchers in recent decades have made and are making a huge effort to develop more autonomous robots, that is, robots that are much more capable of making decisions by themselves. To reach this goal, it is clear that the first thing to do is improve the sensitive apparatus of the robot, that is, to increase the number of sensors through which the robot can sense the environment in which it operates and diversify the kinds of physical properties it can feel. Tactile sensors are a class of sensors on which the scientific community is focusing. In nature, tactile sensing is an essential tool, especially for human beings. Picking up an object without making it slip and moving in an unstructured time-varying environment is something humans do every moment of their lives: humans' sensing system is designed by nature to work in such conditions, so an approach for building new-generation robots is too look at human beings' sensing system and trying to imitate it in the realization of a robot sensing system. When one considers tactile sensors, it is useful to begin by considering the fundamental physical quantities that can only be sensed through contact with the environment. The most important quantities measured with touch sensors are shape and force.[1–4]

The measurement of contact forces occurring during a manipulation is accomplished with different types of sensors, most often embedded as matrices in an elastic material on the fingertips of an end effect or a manipulator. These individual sensing elements, called *taxels* (the word *taxel* derives from the union of the words *tactile* and *element*), give information about the contact status of the surface on which they are mounted. Although many techniques and technologies have been used to build tactile sensors, very little commercial success has been obtained so far. The complexity of many of the current technologies makes them hard to manufacture, and thus, they are very costly. The following list provides a general description of the most common sensor configurations. A more comprehensive review can be found in ref. 5:

1. Resistive sensors: These devices are usually divided in two subgroups. The sensors of the first subgroup exploit the force-resistance characteristic of conductive elastomers and foams. When subjected to an external force, these

*Correspondence to:* L. Grassia (luigi.grassia@unina2.it).
Contract grant sponsor: European Community's Seventh Framework Programme (FP7/2007-2013); contract grant number: 216239 (DEXMART project).

materials exhibit a predictable loss of electrical resistivity. The sensors are sandwiched between layers of polyester film, on which conductive grids are printed. The intersection points of rows and columns of the grid form sensing sites. Conventionally, the sensors based on the use of strain gauges also fall in this category. Recently, Tarchanidis and Lygouras[6] mounted strain gauges on a steel surface and built a sensor for small forces ($\leq$0.38 N) with a linear response and sensitivity of 0.05 V/N; the sensor was mountable on a data glove. In 2007, Hwang et al.[7] used strain gauges, integrating four of them into a polymer substrate; the sensing area of the resulting taxel was $1 \times 1$ mm$^2$. It could measure up to 4-N normal forces and had the capability of measuring tangential forces, too. An example of the integration of a tactile sensor onto a robotic hand can be found in ref. [8]. Here, a conductive rubber was used to obtain a sensor with a sensing area of $0.5 \times 3$ mm$^2$ and a measurement range of 0–0.2 MPa. However, the pressure-conductive rubber had a hysteresis effect, in which the relationship between the stress and resistance values showed a loop at the time pressure was applied and removed. As a result, the measured values differed from the loading sequence. A *force-sensing resistor* is a piezoresistive polymeric material that exhibits decreased resistance when pressure is applied normal to its surface. A film consisting of electrically conducting and nonconducting particles suspended in a matrix is etched onto facing surfaces of pliable polymer sheets. The electrical resistance between the conductors is measured through the force-sensing resistor polymer. Piezoresistive technology is probably the most used technology for creating tactile sensors, especially when the dimensions of the sensor are an important design parameter, thanks to the possibility of integration on a silicon wafer. An example of a very small sensor, with a volume of $200 \times 200 \times 8$ $\mu$m$^3$, and for very small forces (it works within the range 0–300 $\mu$N), can be found in ref. [9]. Another interesting example of a piezoresistive sensor is the one described in ref. [10]; although the taxel dimensions were large for such a sensor (the single taxel measured $2.3 \times 2.3 \times 1.3$ mm$^3$), it could measure both normal, up to 2 N, and tangential forces, up to 0.7 N. Although the characteristics of this sensor were monotonic, it was featured with hysteresis.

2. Piezoelectric sensors: Materials convert mechanical stress into proportional output voltage potentials. A typical example of a piezoelectric sensor is the one proposed in ref. [11]. The sensing area was $5 \times 7.5$ mm$^2$, and it responded with a potential difference of 0–8 V for pressures on it of 0–75 kPa. An innovative way of using piezoelectric materials to create a tactile sensor was shown in ref. [12], as this sensor was based not on the capability of the piezoelectric material of generating a potential difference when mechanically shocked but on the variation of the resonance frequency of the piezoelectric device caused by the application of a pressure.
3. Capacitive sensors: These sensors rely on the fact that the capacitance of a parallel-plate capacitor is a function of the thickness of the medium between the plates. Such devices respond to applied forces that change this distance. Capacitive sensors, like piezoresistive ones, have been widely used when the dimensions of the sensors have been important, thanks to the possibility of creating silicon integrated capacitors. Two examples may be found in ref. [13], where two sensors were realized with a maximum sensing area of $154 \times 154$ $\mu$m$^2$ and which were capable of sensing pressures from $-1000$ to 3000 hPa. The sensor proposed in ref. [14] used variation of the thickness of the medium between the plates of a cylindrical capacitor to sense radial forces. It was a big sensor, with a diameter of 15 mm and a height of 20 mm and could measure forces up to 11.76 N.
4. Magnetic sensors: Transduction sensors rely on mechanical movements to produce flux density changes in magnetic fields. These measurements are usually made by Hall effect sensors. Other such transducers employ magnetoresistive or magnetoelastic materials, which, if subjected to mechanical stress, change their magnetic fields. Again, in ref. [14], the variation of magnetic flux was exploited to determine the axial force, up to 4 N.
5. Photoelectric or optical sensors: These sensors exploit the electromagnetic properties of light. Widely used sensors are based on fiber Bragg gratings (FBGs). Typical examples are the two sensors discussed in ref. [15]. It was shown how it is possible to use FBGs to create both big and small sensors. The single taxel of the big sensor had dimensions of $15 \times 15 \times 10$ mm$^3$, showed a monotonically increasing characteristic (change in the wavelength at the output of the FBG vs force applied), and could sense forces up to 5 N. The small sensor had sensing area dimensions of $4 \times 2$ mm$^2$, again had a monotonically increasing characteristic, and could sense forces up to 10 N. In both cases, when the array of sensors was created, an

interference test was performed; that is, a load was applied on only one of the taxels, and the output of all of the other taxels was measured. Other sensors were based on scattering by small or big particles (cf. the wavelength used) and made use of highly scattering materials, such as foams. An example of how foams can be used can be found in ref. [16], where the urethane foam was inserted inside a cavity whose dimensions varied according to the external force applied. When the cavity was compressed, the scattered energy density varied. Through the detection of this variation, it was possible to sense how the dimensions of the cavity changed, and through knowledge of the mechanical properties of the cavity, it was possible to reconstruct what the force compressing the cavity was. This made the range and sensitivity easily adjustable through changes in the material of the cavity and/or the scattering material inside the cavity. Urethane foam was also used in ref. [4], where an entire skin, with dimensions of 120 $\times$ 200 mm$^2$, was developed, with a nonlinear hysteretic response going from 1 to 3 V for pressures applied in the range 0–50 kPa.

## SENSOR CONCEPT

The tactile sensor concept proposed in this article was based on the use of optoelectronic technologies. As mentioned, existing solutions exploit light propagation in scattering materials. Their main drawback is related to the stochastic nature of the scattering phenomenon; therefore, the measurement process is characterized by a lack of repeatability. Moreover, all of these sensors are sensitive only to the normal components of the contact force vector, or they cannot distinguish between the effects caused by normal and tangential components. To avoid the former problem related to scattering, in the proposed sensor, the entire light path from the source to the receiver was in air. To measure both normal and tangential components of the contact force vector, a deformable elastic layer was positioned above the optoelectronics devices to act as a transducer of forces into displacements, which were then measured as explained in the following.

In sum, the objective of the proposed sensor was to provide information about the contact point/area between the fingertips and the manipulated object, together with an estimate of both the normal and tangential components of the contact force. Researchers working on the development of innovative tactile sensors too often neglect the estimation of the tangential component, but it is essential to correctly implement manipulation tasks.

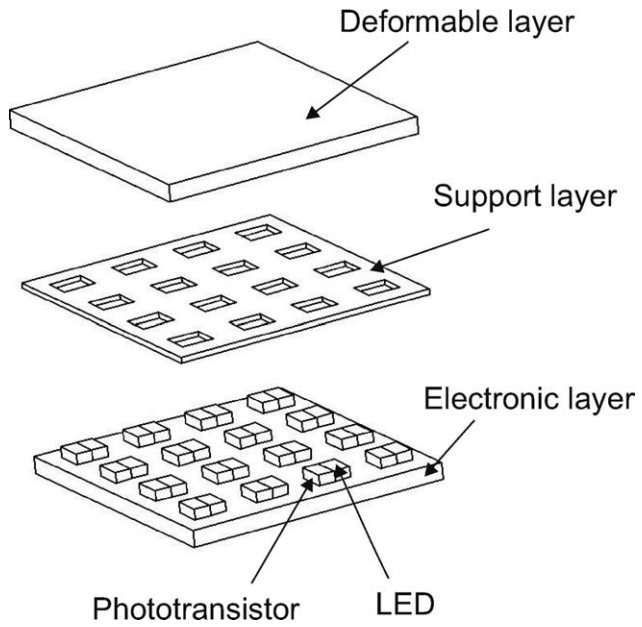


**Figure 1** Structure of the tactile sensor.

The proposed tactile sensor was based on the use of light-emitting diode (LED)–phototransistor couples and a deformable elastic layer positioned above the optoelectronics devices (see Fig. 1). A support layer was used to fix the initial distance between the electronic layer and the deformable layer to optimize the sensitivity and also to avoid cross-talk disturbances. The optoelectronic components were organized in a matrix structure. For each couple, the LED illuminated the reflective surface, which coincided with the bottom facet of the deformable layer. Practically, the deformable layer transduced an external force into a displacement variation of its bottom facet through its stiffness. An external force applied to the deformable layer produced local variations of the bottom surface of the elastic material, and the couples of optical devices measured the vertical deformations in a discrete number of points. In particular, these vertical displacements produced a variation of the reflected light intensity and, accordingly, of the photocurrent measured by the photodetector. The vertical displacements, measured for each taxel, could be positive or negative; that is, the deformable layer could locally go up or down (see Fig. 2), depending on the amplitudes of the tangential and normal force components. Finite element (FE) analysis, detailed in the following section, demonstrated that the latter relationship could be used to actually reconstruct the external force components through measurement of the elastic layer vertical deformation in a discrete number of points.

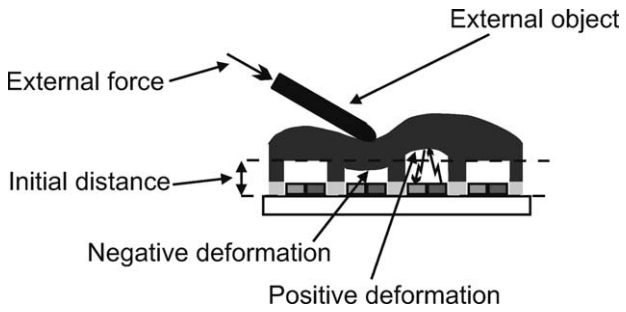


**Figure 2** Sketch of the working principle.

## EXPERIMENTAL

Two different prototypes of the tactile sensor were made. The smaller one consisted of 4 × 1 taxels and served to validate the sensor concept. The bigger one consisted of 4 × 4 taxels and was able to cover a sensing area similar in terms of dimensions and shape to a human fingertip.

The deformable layer of the sensor prototype was made of black silicone rubber to avoid cross-talk problems and ambient light disturbances because the black color guaranteed the maximum absorption for every wavelength. Only the surface facing each device pair was white, to increase the sensor sensitivity and ensure the maximum reflection for every wavelength. Silicone rubber MM906 provided by ACC Silicones Europe (Milan, Italy) (Shore hardness 6A) was used as a deformable layer material of the tactile sensors. This was a two-component, room-temperature, condensation-curing silicone compound. The rubber was cured for 24 h before use. To prevent imperfections due to air bubbles in the cured rubber, the liquid rubber was deaerated with intermittent evacuation for 1 h *in vacuo*.

Axial stress (σ)–strain tests were carried out on the silicone material with a Zwick-Roell (Genova, Italy) Z10 test machine equipped with a BTC-EXMA-CRO.001 extensometer according to an ASTM standard. In Figure 3, the results of the axial test are reported. It can be readily observed that a steady-state stress–strain curve area was obtained after the second cycle of deformation. Furthermore, the rubber material showed a little hysteresis after the first cycle of loading. The silicone rubber behavior was modeled with the Mooney–Rivlin constitutive law:

$$\sigma = 2\left(\lambda - 1/\lambda^2\right)(\alpha_1 + \alpha_2/\lambda) \qquad (1)$$

where λ is the elongation ratio. The model parameters ($\alpha_1 = 3.96 \times 10^{-2}$ and $\alpha_2 = -3.37 \times 10^{-4}$) were evaluated by the fitting of the experimental stress–strain data acquired during the third cycle of loading. The results of the fitting procedure are displayed in Figure 4, where the experimental data are

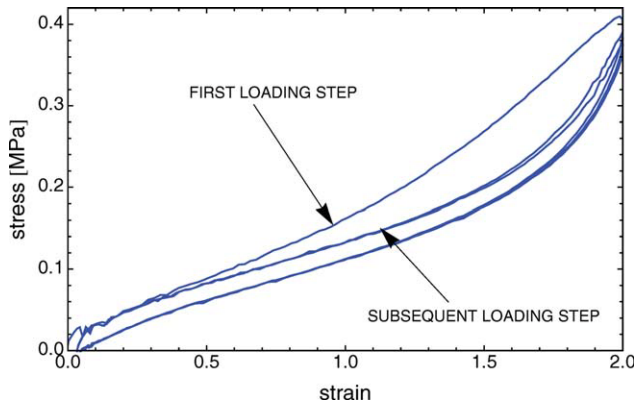


**Figure 3** σ–strain behavior of the silicone rubber used as deformable layer in the tactile sensor. [Color figure can be viewed in the online issue, which is available at wileyonlinelibrary.com.]

reported as symbols and the Mooney–Rivlin model prediction is reported as a solid line.

The realized prototypes used optoelectronic components manufactured by OSRAM. The LED (code SFH480) was an infrared emitter with a typical peak wavelength of 880 nm, and the detector was a silicon negative-positive-negative (NPN) phototransistor (code SFH3010) with a maximum peak sensitivity at a wavelength of 860 nm. Both of the components had a viewing angle of ±80°. It is worth mentioning that the optoelectronic components had very large viewing angles to minimize the effects of the LED radiation pattern and photodetector responsivity pattern on the photocurrent and to leave only the dependence with distance. The conditioning electronics were only constituted by simple resistors without amplification and/or filtering blocks. As a result, the collector current of the phototransistors, depending on the received light intensity, was easily translated into a voltage signal via a suitable resistor. The voltage supply of the component matrix

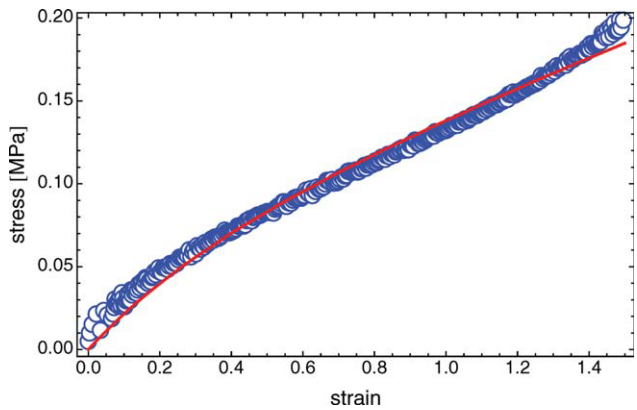


**Figure 4** Stress versus strain in the third cycle of loading. The symbols indicate experimental data, and the solid line indicates Mooney–Rivlin model prediction. [Color figure can be viewed in the online issue, which is available at wileyonlinelibrary.com.]

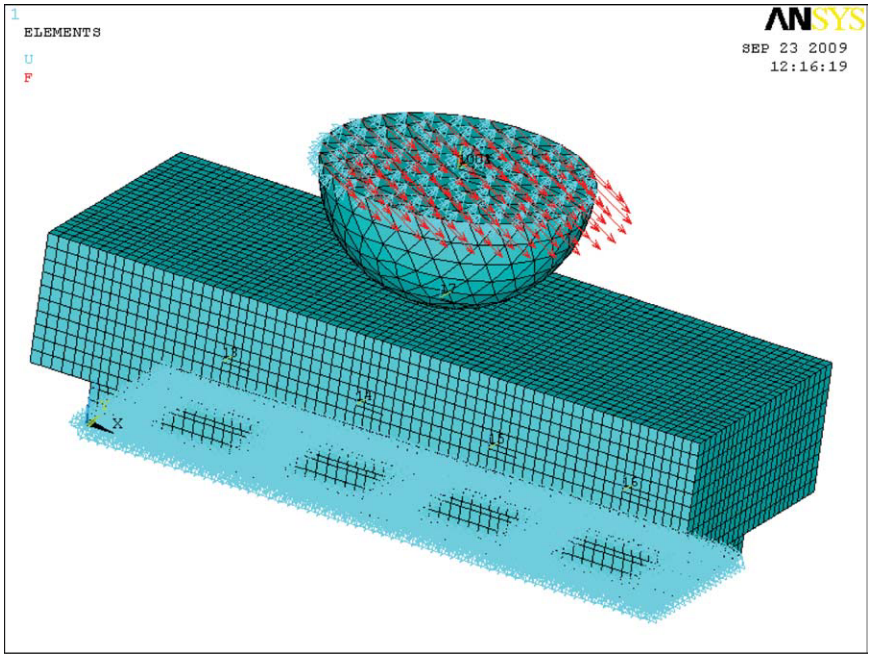


**Figure 5** FE model of the 4 × 1 taxel sensor. [Color figure can be viewed in the online issue, which is available at wileyonlinelibrary.com.]

was 5 V. Each LED was used with a forward current of less than 5 mA, with a maximum power consumption of less than 200 mW for the whole sensor.

### FE analysis

The silicone rubber deformable layer was modeled (see Fig. 5 for the 4 × 1 taxel sensor and Figure 6 for the 4 × 4 taxel sensor) with brick elements with 3 degrees of freedom for each node (element 185 from the ANSYS element library). For the sake of simplicity, in this first phase, a single spherical contact was considered. It should be noted that the shape of the contact surface could be neglected when the silicone layer thickened whereas the size of the contact area was take into account in the next phase. The contact interface between the spherical punch and the

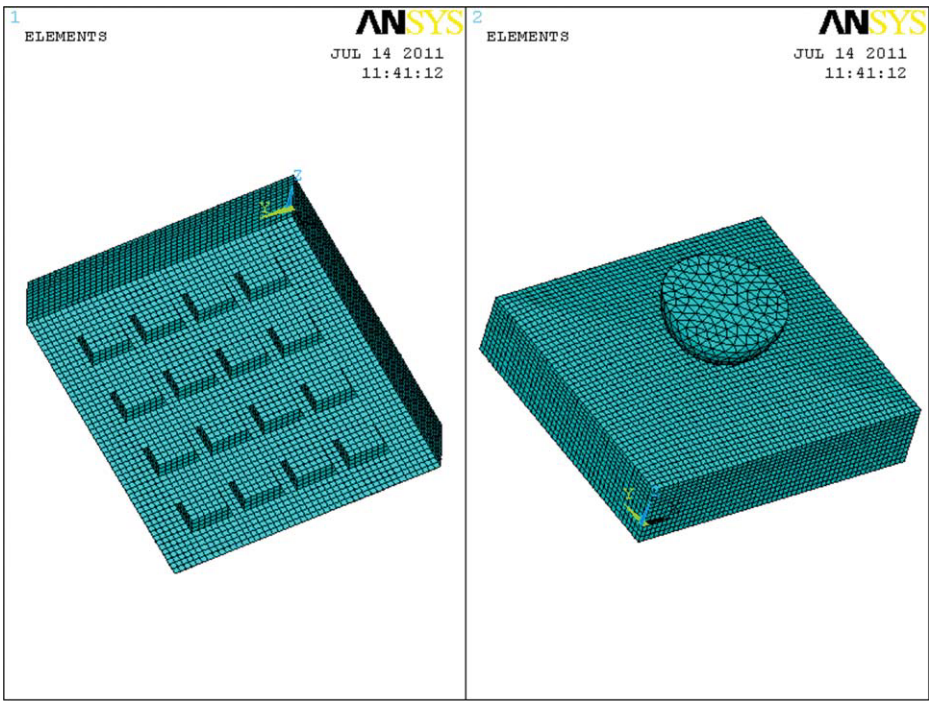


**Figure 6** FE model of the 4 × 4 taxel sensor. [Color figure can be viewed in the online issue, which is available at wileyonlinelibrary.com.]

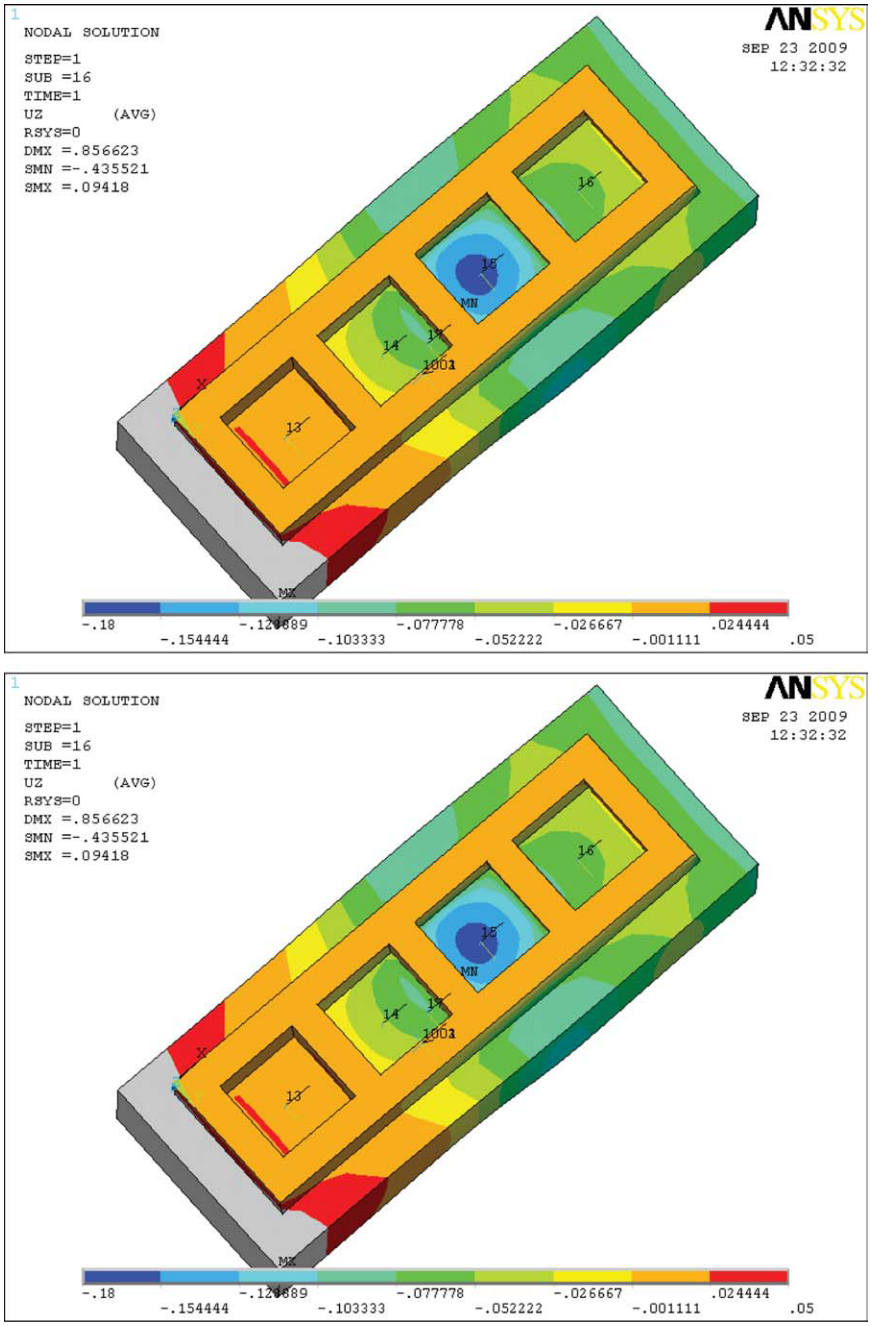


**Figure 7** Contours of the vertical displacements for the 4 × 1 taxel sensor: (a) the force was applied normally to the deformable layer surface (θ = 90°) and (b) the force contained both normal and tangential components (θ = 30°). [Color figure can be viewed in the online issue, which is available at wileyonlinelibrary.com.]

deformable layer was modeled with the soft penalty method.

In Figure 7(a,b), the vertical displacements resulting from the FE analysis performed on the 4 × 1 taxel sensor are reported. In Figure 7(a), the force was applied normally to the deformable layer surface (θ = 90°, where θ is the angle between the force direction and the deformable layer surface), whereas in Figure 7(b), the applied force contained both normal and tangential components (θ = 30°). For both cases, the position of the applied force ($p$) was the center of the deformable layer ($p$ = 0 mm), and its amplitude was 0.2 N. Figure 7(a,b) shows that the degree of asymmetry increased with decreasing θ. In particular, the application of a force with a tangential component different from zero gave rise to both negative and positive vertical displacements, whereas the application of a purely normal force gave rise only to negative vertical displacement. This feature suggested that the measurement of the vertical displacement in the

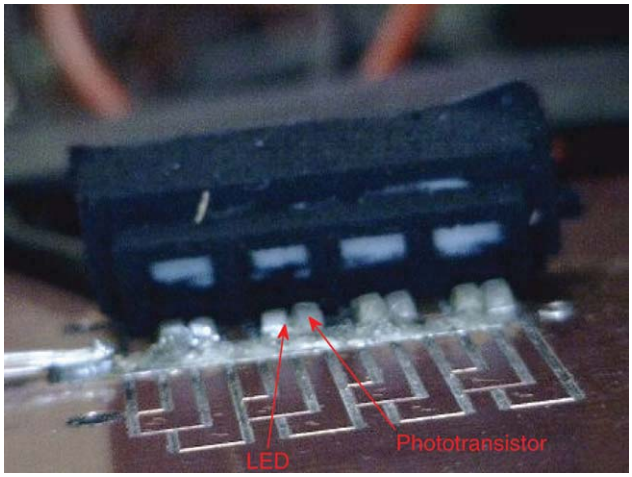


**Figure 8** Tactile sensor prototype with four taxels in line. [Color figure can be viewed in the online issue, which is available at wileyonlinelibrary.com.]

discrete number of points should have been enough to estimate all of the force components.

Further, it is worth mention that the tangential components of the applied force caused nonsymmetric horizontal displacements of the deformable layer. This means that the deformed shape of each cell was a nonorthogonal hexahedron, and consequently, the effective reflecting surface was diminished. To avoid this behavior, the vertical walls of each cell were dimensioned in a way such that the $x$–$y$ displacements did not overcome one-tenth of the cell height.

## Validation of the FE model

The numerical model was experimentally validated by a set of experimental measurements on a 4 × 1 taxel prototype (see Fig. 8) with the same geometry and material considered in the FE model.

The first step of the numerical/experimental correlation was to obtain a relationship between the photocurrent of the phototransistor and the displacement of the bottom facet of the elastic layer of each taxel. As mentioned, a change in the distance between the receiver LED phototransistor and the reflecting facet caused photocurrent variations. This is a well-known consequence of electromagnetic field propagation laws. However, a closed-form expression of the light intensity as a function of this distance was very difficult to obtain, especially because of the small entity of this distance, which was far below the inferior limit for the far-field region condition, as given by

$$r > \frac{L_{\max}^2}{\lambda} \tag{2}$$

where $r$ is the distance between the electromagnetic source and the point where the field is measured; $L_{\max}$ is the diameter of the detector and $\lambda$ is the wavelength of the emitted light. For the optoelectronic components at hand, the parameters were such that this limit was about 240 mm. Therefore, the displacement/voltage relationship was experimentally obtained one taxel at a time.

The FE numerical model was experimentally validated with the application of external forces with a constant module (0.2 N) in the center of the smallest prototype with different angles. Figure 9 presents the comparison between the measurements and the numerical predictions in terms of vertical displacements for each taxel. The vertical displacement obtained numerically and reported in Figure 9 represents the mean performed on the area of each

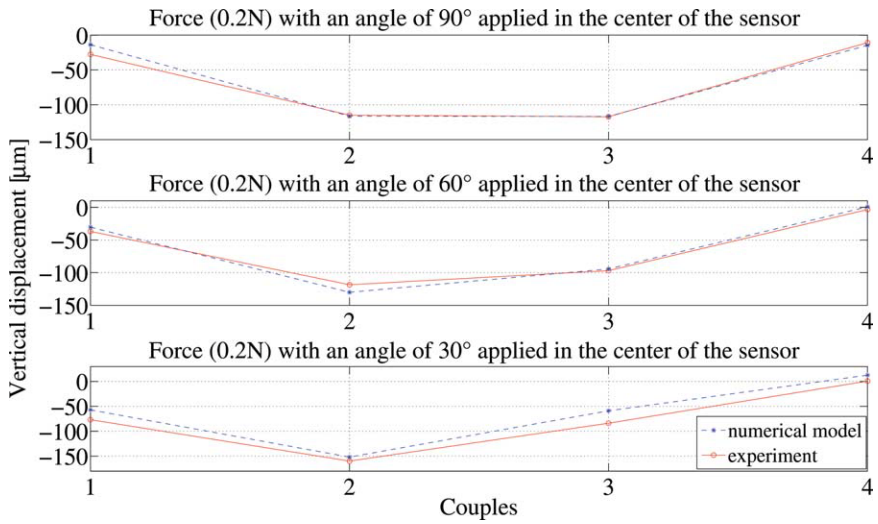


**Figure 9** Comparison between the experimentally measured and the FE calculated vertical displacements for the 4 × 1 taxel sensor. [Color figure can be viewed in the online issue, which is available at wileyonlinelibrary.com.]

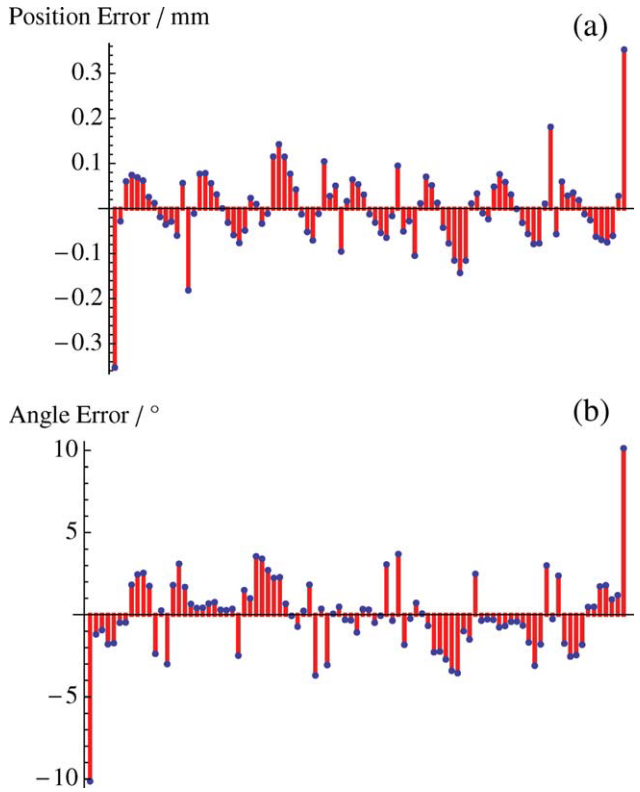


**Figure 10** Error of estimation of (a) the contact point position and (b) the angle of the applied force for the data used in the fitting procedure. [Color figure can be viewed in the online issue, which is available at wileyonlinelibrary.com.]

reflecting facet. The results show a good correlation between the experimental measurements and the numerical solution, although slight deviations were observed as the tangential component of the applied force increased.

## Validation of the sensor concept

A parametric FE analysis was carried out on the smallest sensor (4 × 1 taxels) by the variation of θ and $p$ of the contact force to check if it was possible to evaluate the contact force, with both tangential and normal components, from the knowledge of the vertical displacement of each reflecting facet. In other words, the parametric analysis served to establish whether it was possible to correlate in a unique way $p$ and θ of the contact force to the set of the mean vertical displacement of each taxel ($u_1$, $u_2$, $u_3$, and $u_4$). To build the data set, the FE analysis was performed by variation of θ between 30 and 150° with a step of 10°, whereas the position was varied between −3 and 3 mm with a step of 1 mm. We also used the FE model to realize a trial set, obtaining the intermediate solutions with respect to the data set.

To minimize the parameter number, $u_1$, $u_2$, $u_3$, and $u_4$ were arranged in such a way to give two quantities, namely $s$ and $t$, that showed a low correlation coefficient (−0.68), as follows:

$$s = -1.5u_1 - 0.5u_2 + 0.5u_3 + 1.5u_4 \tag{3}$$

$$t = u_1u_3 - u_2u_4 \tag{4}$$

It was assumed that $p$ and θ were odd polynomial functions of $s$ and $t$, as follows:

$$p(s,t) = a_1s + a_2t + a_3st^2 + a_4s^2t + a_5s^3 + a_6t^3 + a_7s^5 + a_8t^5 \tag{5}$$

$$\theta(s,t) - 90^\circ = b_1s + b_2t + b_3st^2 + b_4s^2t + b_5s^3 + b_6t^3 + b_7s^5 + b_8t^5 \tag{6}$$

A fitting procedure based on the Marquardt–Levenberg algorithm was used to find the 16 best-fit parameters ($a_1$, …, $a_8$ and $b_1$, …, $b_8$). The results of the fitting procedure are displayed in Figure 10(a,b) in terms of errors in the position and the angle, respectively. The model was also tested with respect to the trial set, and the results are reported in Figure 11(a,b), again in terms of errors in the position and the angle,

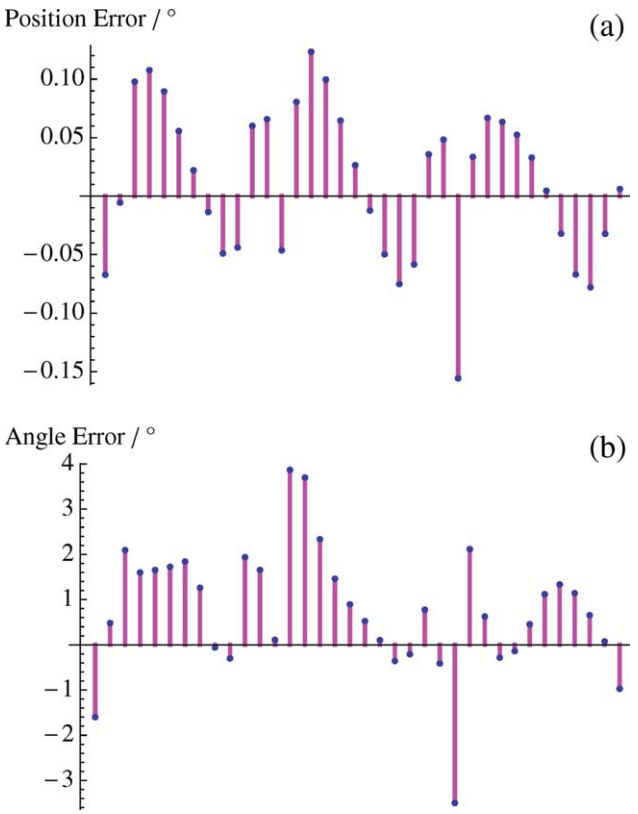


**Figure 11** Error of estimation of (a) the contact point position and (b) the angle of the applied force for the trial set data. [Color figure can be viewed in the online issue, which is available at wileyonlinelibrary.com.]

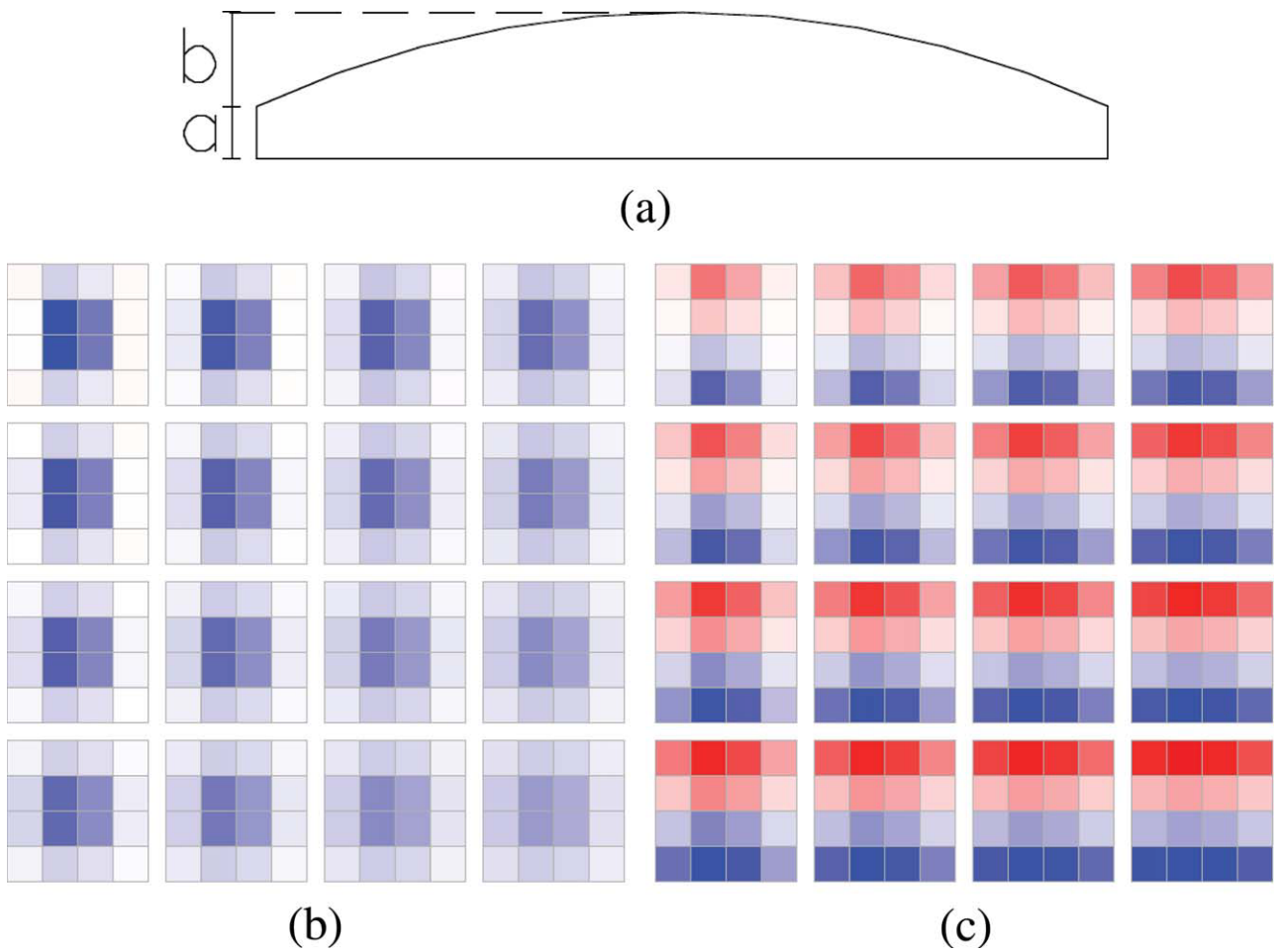


**Figure 12** Taxels mean vertical displacement with variations of parameters *a* and *b*.

respectively. It appeared that the model predicted quite well both the position and the angle, with a maximum error for the angle of less than 10° and with a maximum error in the position of 0.3 mm.

This means that it was possible to reconstruct the contact force from the information related to the mean vertical displacement of each taxel; that is, the proposed sensor concept was adequate to deal with the tactile problem.

### Optimization of the deformable layer shape

The results of the analysis described in the previous section encouraged starting the design of an actual tactile sensor able to cover an entire sensing area similar in terms of dimensions and shape to the human fingertip. Hence, a more complex FE model of the deformable layer was set up also by complication of the geometry of the contact surface. As a first attempt, the geometry of the cross-sectional area of the deformable layer was assumed to be constituted by a portion of a circular segment placed over a rectangle, as depicted in Figure 12(a), which shows the FE model of the deformable layer.

As verified in the analysis described so far, the geometry of the deformable layer played a key role in establishing the sensitivity of the sensor; hence, a parametric FE analysis was carried out to select the geometry to obtain a satisfactory sensitivity to both the normal and tangential components of the contact force vector. The parametric analysis was performed by variation of the thickness of the rectangle (*a*) and the height of the circular segment (*b*).

The results of the analysis, in terms of the mean vertical displacement for each cell when a normal or a tangential force was applied, are reported in Figure 12(b,c), respectively. Furthermore, the rows and columns indicated an increase of parameters *a* and *b*, respectively, starting from the top left corner. The red color indicates upward displacement, whereas the blue one indicates downward displacement. The color intensity is proportional to the displacement value. From Figure 12(b) (normal force), it appears that as long as $a + b$ increased, the pattern of the vertical displacement became uniform and less intensive, whereas when a tangential force was applied [see Fig. 12(c)], as long as $a + b$ increased, the mean vertical displacement in each cell

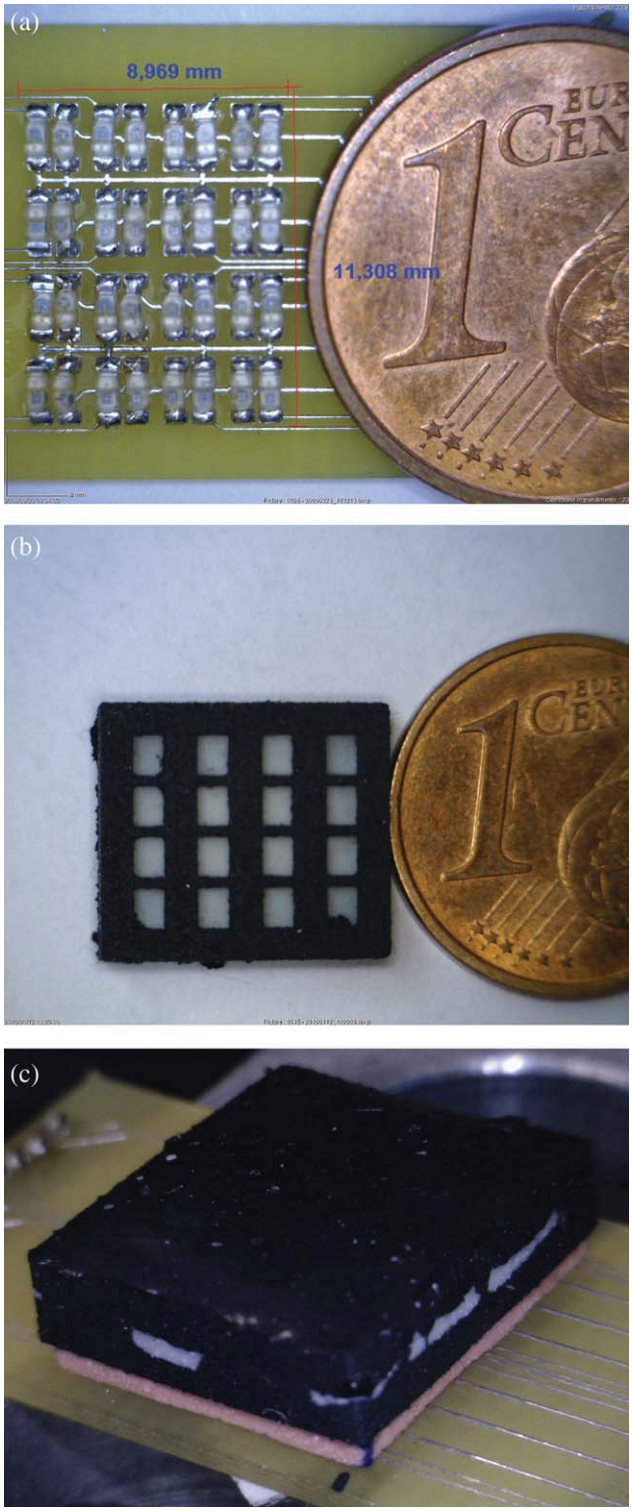


**Figure 13** Some pictures of the final prototype: (a) electronic layer, (b) deformable layer, and (c) complete sensor. [Color figure can be viewed in the online issue, which is available at wileyonlinelibrary.com.]

increased. We could explain this last feature by taking into account that the moment of the tangential force increased with $a + b$. Consequently, from the normal force point of view, the optimal geometry configuration was characterized by the minimum value of $a + b$, whereas from the tangential force point of view, the optimal geometry coincided with the maximum value of $a + b$. Obviously, the final choice would be a trade-off between the two extreme configurations.

## CALIBRATION OF THE 4 × 4 TAXEL SENSOR PROTOTYPE

We realized the final sensor prototype (see Fig. 13), from the mechanical point of view, by taking into account the results of the FE analysis and the experimental measurements carried out on the 4 × 1 taxel prototype. The expected measurement range of the sensor was 2 N. The maximum force level could be improved simply by a change in the hardness of the deformable layer. The maximum measurable force was limited by the maximum vertical deformation of the reflective surface of each taxel, so the former could be improved by an increase in the stiffness of the deformable layer. A linear relation between the Shore hardness and the logarithm of the Young's modulus was derived in ref. [18] for elastomeric materials. With this relation, the maximum predictable force level went from 2 to 40 N when the hardness of the deformable layer was changed from 6 to 60 Shore A.

Figure 14 shows a sketch of the sensor, where the position of each cell with respect to the reference axes is indicated. The position of the $k$th taxel could be identified with a couple of coordinates ($x_k$, $y_k$), which refer to the center position of the $k$th taxel. When an external force was applied to the sensor,

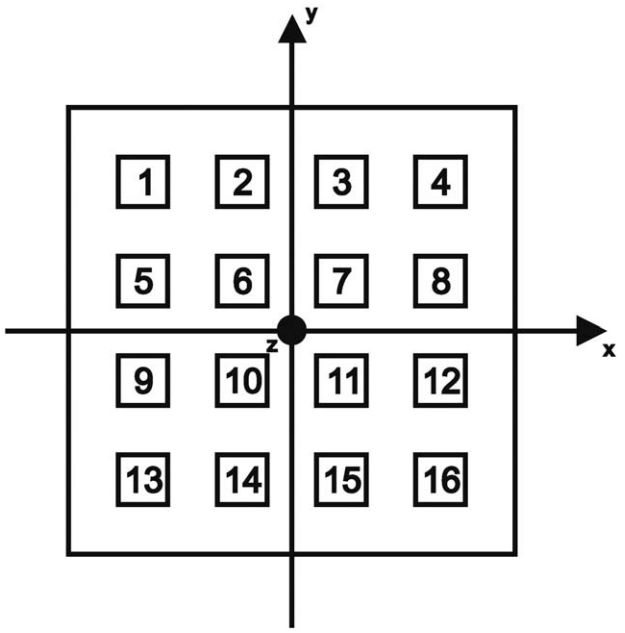


**Figure 14** Scheme of the sensor taxels with respect to the reference axes.

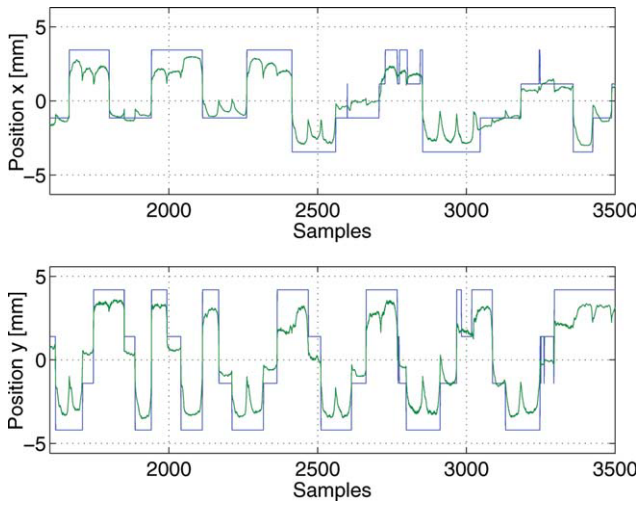


**Figure 15** Estimated contact point position with the two proposed methods. Blue line: first method; green line: second method. [Color figure can be viewed in the online issue, which is available at wileyonlinelibrary.com.]

the distance of the reflecting surface of each cell from the corresponding LED/phototransistor couple on the electronic layer could be subjected (as shown by the FE analysis described in the previous sections) to a positive or a negative variation. These distance variations implied changes in the reflected light and, accordingly, in the voltages measured by the phototransistors. With $c_k$ defined as the voltage variation for the $k$th taxel, $c_k > 0$ denotes an increasing distance, whereas $c_k < 0$ denotes a decreasing distance between the reflecting surface and the electronic layer (obviously, $c_k = 0$ denotes no variation). The taxels that presented $c_k < 0$ provided information about the contact point/area, whereas all of the taxels with $c_k \neq 0$ provided information about the amplitudes of the normal and tangential force components. In particular, the cells with $c_k > 0$ indicated the presence of a tangential force component. As a result, the calibration of the prototype was carried out in two steps. In the first step, the estimation of the contact point was tackled. The simplest possible solution was based on the idea of approximating the contact point position with the coordinates $(x_k, y_k)$ of the taxel corresponding to the minimum measured $c_k$ value, namely

$$\begin{cases} \hat{x} = x_k \\ \hat{y} = y_k \end{cases} \quad k = \min_{h=1,\ldots 16} c_h \tag{7}$$

where (◯, ŷ) are the estimated coordinates of the contact point. The advantage of this solution was its simplicity, but the disadvantage was that the estimated position was limited to a discrete number of points and the resolution depended on the relative distances between the taxels. To obtain a better estimation of the contact point position, a second method was investigated. The proposed solution used all of the data of $c_k < 0$ to estimate the contact point coordinates, that is

$$\hat{x} = \frac{\sum_{k=1}^{16} x_k F(c_k)}{\sum_{k=1}^{16} F(c_k)} \quad \hat{y} = \frac{\sum_{k=1}^{16} y_k F(c_k)}{\sum_{k=1}^{16} F(c_k)} \tag{8}$$

where

$$F(c_k) = \begin{cases} c_k & \text{if} \quad c_k \leq 0 \\ 0 & \text{if} \quad c_k > 0 \end{cases} \quad k = 1, \ldots, 16 \tag{9}$$

This second method was similar to a center-of-mass estimation, and it allowed us to achieve a subtaxel resolution. The selection of the method to use can be adaptive with respect to the manipulated object. Both of the solutions were valid under the assumption of a single contact. The multiple-contact case will be the subject of future investigation. Figure 15 shows the results of the contact point position

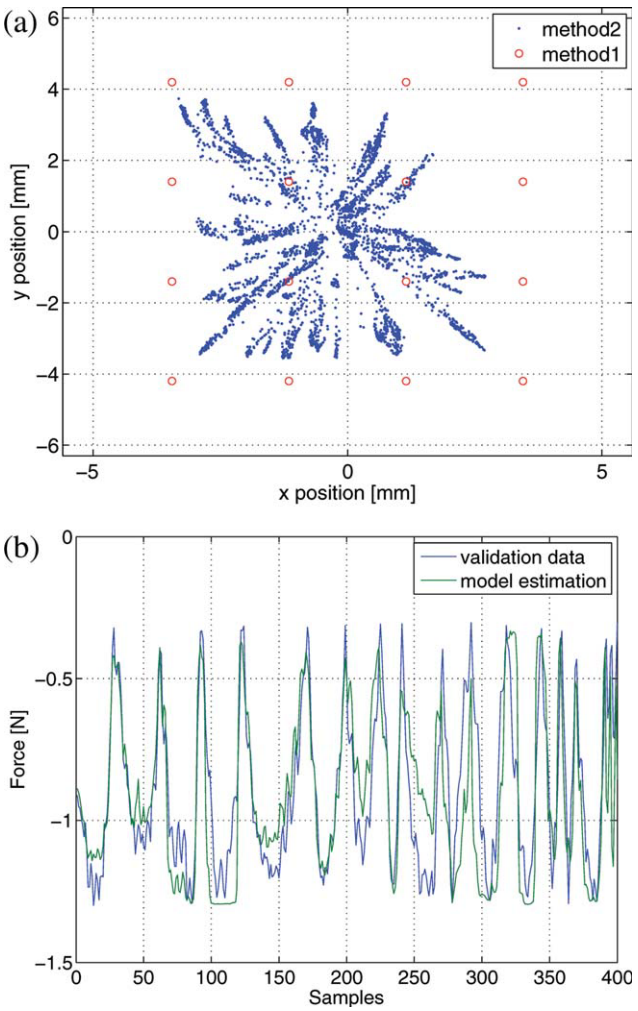


**Figure 16** Calibration results with forces applied normally on the whole sensor surface: (a) contact point position and (b) contact force modulus. [Color figure can be viewed in the online issue, which is available at wileyonlinelibrary.com.]

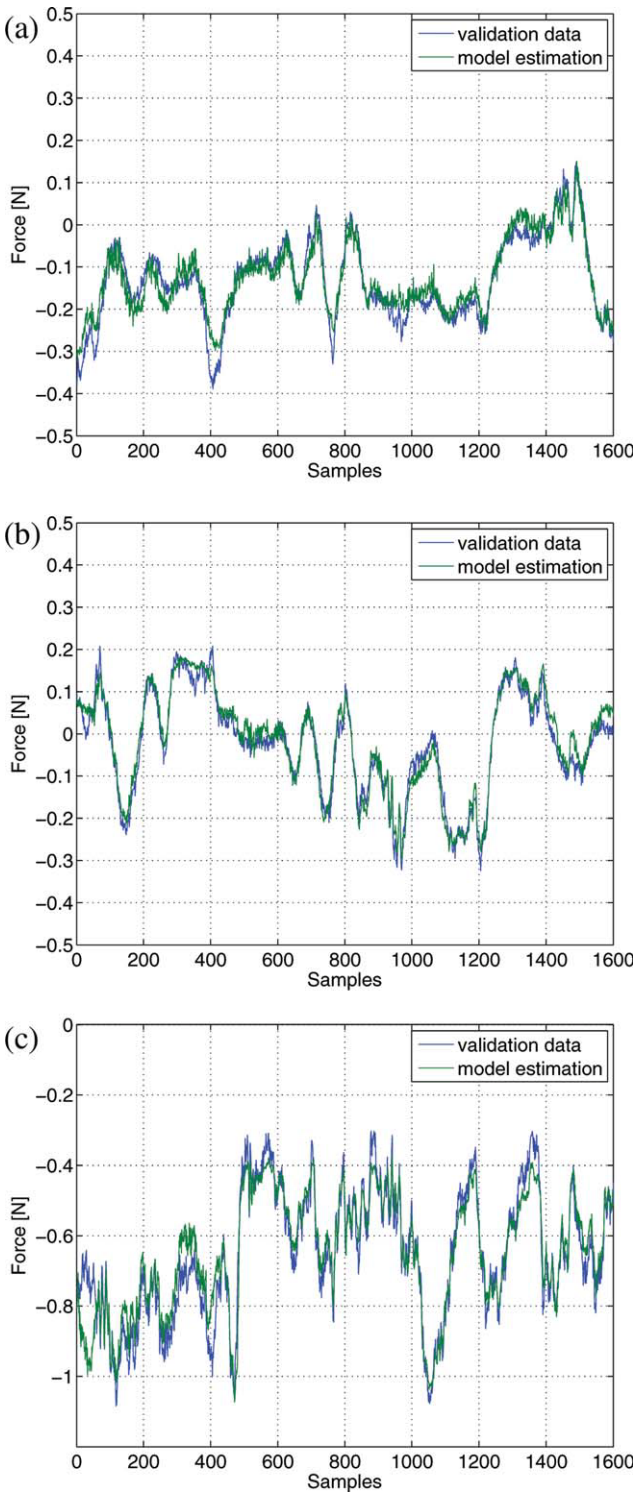


**Figure 17** Calibration results with normal and tangential forces applied only on the central area of the sensor: (a) force component along the $x$ axis, (b) force component along the $y$ axis, and (c) force component along the $z$ axis (c). [Color figure can be viewed in the online issue, which is available at wileyonlinelibrary.com.]

estimation with the two proposed methods. Evidently, the first method led to discrete values for the estimated position.

The second step concerned the estimation of the applied external force components. The proposed approach was based on the use of a neural network to interpolate a number of data sufficient to model the relationship between the applied forces and the phototransistors measurements. The prototype was mounted on a six-axis load cell used as a reference sensor. We carried out various experiments by applying different external forces and simultaneously acquiring all of the voltages on the phototransistors and all the force components measured by the load cell. These data were organized in a training set to be used as input data (voltages) and target data (forces) of the neural network and a validation set to assess the trained network. We addressed the problem by taking into account the following aspects. The normal force component mainly depended on the taxels with $c_k < 0$, which coincided with the closest ones to the contact point. On the contrary, the tangential force components depended on the taxels with $c_k > 0$, which were the cells adjacent to the previous ones. This means that the estimation of the normal force was expected to be accurate over the entire available surface of the sensor, whereas the accuracy of the tangential component reconstruction was expected to decay when the contact point moved away from the central area of the sensor surface. As a result, the sensor was calibrated by the consideration of two different cases: only normal forces applied on the whole sensor surface and both normal and tangential forces applied on the central area of the sensor. The forces were applied with a punch with a contact surface smaller than the sensor surface. A standard two-layer, feed-forward neural network, trained with the Levenberg–Marquardt method, was used in both cases. The first one, with only normal forces, was modeled with 12 neurons for the hidden layer and 1 for the output layer. For the second case, the number of hidden layer neurons was set to be equal to 16, whereas the neurons for the output layer were fixed at 3. The results of the first calibration are reported in Figure 16, together with the map of the corresponding estimated positions. The reconstructed force components in the second case are reported in Figure 17. A map of the positions estimated in the latter case is reported in Figure 18. In both cases, the reconstruction performance of the neural network was quite satisfactory.

## CONCLUSIONS

This article presents a novel tactile sensor concept based on an electronic layer constituted by discrete LED/phototransistor couples used in combination with a silicone rubber deformable layer. An intensive FE analysis was carried out to validate the

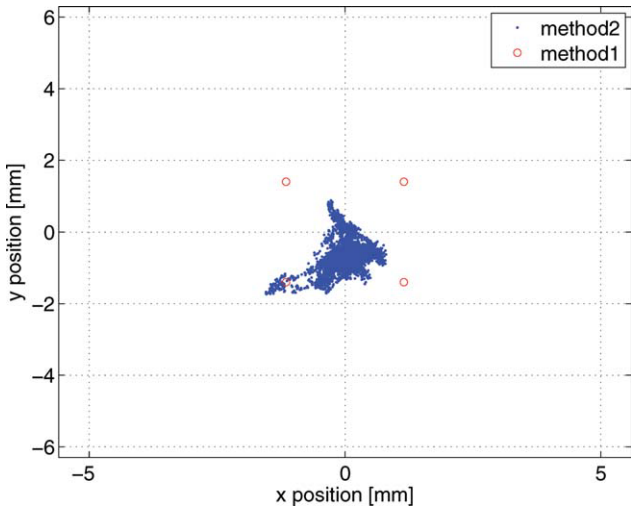


**Figure 18** Map of the estimated contact point position corresponding to the estimated forces reported in Figure 17. [Color figure can be viewed in the online issue, which is available at wileyonlinelibrary.com.]

sensor concept and to select the sensor geometry with the best sensitivity to both the normal and tangential components of the contact force. A calibration technique was used to estimate both the contact point position and the components of the applied force. Nevertheless, a number of issues still need attention and further investigation. With regard to the mounting of the optoelectronic components, misalignment of their optical axes caused coupling between adjacent taxels, and thus, optimization of the mounting procedure should be sought. This limitation could be overcome by integration of the taxel matrix into a single integrated circuit with different electronic technologies, for example, organic electronics. Another improvement of the sensor would be a better spatial distribution of the taxels, different from the simple matrix structure. Finally, more sophisticated calibration procedures could be investigated, both model-based and phenomenological, which could be possibly automated.

## References

1. Siciliano, B.; Khatib, O. Springer Handbook of Robotics; Springer: New York, 2008.
2. Lee, M. H.; Nicholls, H. R. Mechatronics 1999, 9, 1.
3. Harmon, L. D. Int J Robotics Res 1982, 1, 3.
4. Ohmura, Y.; Kuniyoshi, Y.; Nagakubo, A. Proc 2006 IEEE Int Conf Robotics Automation 2006, May, 1348.
5. Dahiya, R. S.; Metta, G.; Valle, M.; Metta, G. IEEE Trans Robot 2010, 26, 1.
6. Tarchanidis, K. N.; Lygouras, J. N. IEEE Trans Instrum Meas 2003, 52, 984.
7. Hwang, E.-S.; Seo, J.-H.; Kim, Y.-J. J Microelectromech Syst 2007, 16, 556.
8. Shimojo, M.; Namiki, A.; Ishikawa, M.; Makino, R.; Mabuchi, K. IEEE Sens J 2004, 4, 589.
9. Wisitsoraat, A.; Patthanasetakul, V.; Lomas, T.; Tuantranont, A. Sens Actuators A 2007, 139, 17.
10. Beccai, L.; Roccella, S.; Arena, A.; Valvo, F.; Valdastri, P.; Menciassi, A.; Carrozza, M. C.; Dario, P. Sens Actuators 2005, 120, 370.
11. Motoo, K.; Arai, F.; Fukuda, T. IEEE Sens J 2007, 7, 1044.
12. Krishna, G. M.; Rajanna, K. IEEE Sens J 2004, 4, 691.
13. Salo, T.; Vancura, T.; Bales, H. J Micromech Microeng 2006, 16, 769.
14. Chi, Z.; Shida, K. Sens Actuators 2004, 111, 172.
15. Heo, J.; Chung, J.; Lee, J. Sens Actuators 2006, 126, 312.
16. Hellard, G.; Russell, R. A. In Proceedings of the Australasian Conference on Robotics and Automation; ARAA: Auckland 2002; p 100.
17. Macosko, C. W. Rheology: Principles, Measurement and Applications. VCH: Weinheim, 1994.
18. Qi, H. J.; Joyce, K.; Boyce, M. C. Rubber Chem Technol 2003, 76, 419.